Braz J Phys (2013) 43:86–104
DOI 10.1007/s13538-013-0118-1

GENERAL AND APPLIED PHYSICS

Quantum Discord in Nuclear Magnetic Resonance Systems at Room Temperature

J. Maziero · R. Auccaise · L. C. Céleri · D. O. Soares-Pinto · E. R. deAzevedo · T. J. Bonagamba · R. S. Sarthour · I. S. Oliveira · R. M. Serra

Received: 10 December 2012 / Published online: 26 February 2013

Abstract We review the theoretical and the experimental researches aimed at quantifying or identifying quantum correlations in liquid-state nuclear magnetic resonance (NMR) systems at room temperature. We first overview, at the formal level, a method to determine the quantum discord and its classical counterpart in systems described by a deviation matrix. Next, we describe an experimental implementation of that method. Previous theoretical analysis of quantum discord decoherence had predicted the time dependence of the discord to change suddenly under the influence of phase noise. The experiment attests to the robustness of the effect, sufficient to confirm the theoretical prediction even under the additional influence of a thermal environment. Finally, we discuss an observable witness for the quantumness of correlations in two-qubit systems and its first NMR implementation. Should the nature, not the amount, of the correlation be under scrutiny, the witness offers the most attractive alternative.

Keywords Quantum information · Quantum discord · Nonclassical correlations · Nuclear magnetic resonance

J. Maziero
Universidade Federal do Pampa, Campus Bagé,
96413-170, Bagé, Rio Grande do Sul, Brazil
e-mail: jonasmaziero@gmail.com

R. Auccaise
Empresa Brasileira de Pesquisa Agropecuária,
Rua Jardim Botânico 1024, 22460-000 Rio de Janeiro,
Rio de Janeiro, Brazil

L. C. Céleri
Instituto de Física, Universidade Federal de Goiás,
74.001-970, Goiânia, Goiás, Brazil

D. O. Soares-Pinto · E. R. deAzevedo · T. J. Bonagamba
Instituto de Física de São Carlos,
Universidade de São Paulo, P.O. Box 369,
13560-970 São Carlos, São Paulo, Brazil

R. S. Sarthour · I. S. Oliveira
Centro Brasileiro de Pesquisas Físicas,
Rua Dr. Xavier Sigaud 150, 22290-180 Rio de Janeiro,
Rio de Janeiro, Brazil

R. M. Serra (✉)
Centro de Ciências Naturais e Humanas,
Universidade Federal do ABC, R. Santa Adélia 166,
09210-170 Santo André, São Paulo, Brazil
e-mail: serra@ufabc.edu.br

1 Introduction

1.1 Bell's Inequalities, Entanglement, and the No-Local-Broadcasting Theorem

The study of quantum correlations is among the most active research branches of quantum information science (QIS). The seminal works of Einstein et al. [1] and Schrödinger [2] first drew attention to the subject, in 1935, and placed the nonlocal nature of the correlations at the focus of initial research. The name *entanglement* was coined by Schrödinger [2]. In 1964, rigorous relations among the average values of composite-system observables were presented by Bell [3]. The Bell inequalities, derived under the assumptions of realism and locality, are violated by quantum systems in certain entangled states, which are said to possess nonlocal quantum correlations [4–6].

In 1989, Werner reported a result that unveiled new perspectives in the study of nonclassical correlations in multipartite systems [7]. By defining entanglement operationally as those correlations that cannot be generated via local quantum operations assisted by classical communication, Werner identified entangled states satisfying all Bell inequalities. Another surprise came with the work of Popescu, who showed that with certain nonseparable local states, quantum states allow teleportation with more fidelity than the classical alternatives [8].

The most general quantum operation describing changes of quantum states has the following form, in the operator-sum representation [9]:

$$\mathcal{E}(\rho) = \sum_j K_j \rho K_j^\dagger, \tag{1}$$

where K_j is the Kraus operator acting on the system state space $\mathcal{H}$, which satisfies the inequality

$$\sum_j K_j^\dagger K_j \leq \mathbb{I}, \tag{2}$$

where $\mathbb{I}$ is the identity operator in $\mathcal{H}$.

The equality on the right-hand side of (2) is a sufficient condition for the map $\mathcal{E} : \mathcal{H} \to \mathcal{H}$ to be trace preserving, that is, to insure that $\mathrm{Tr}\,[\mathcal{E}(\rho)] = 1$.

The most general bipartite state that can be created via local quantum operations ($\mathcal{E}_A$ and $\mathcal{E}_B$) and classical communication has the form

$$\rho_{AB}^{\mathrm{sep}} = \sum_j p_j \rho_j^A \otimes \rho_j^B, \tag{3}$$

where $\{p_j\}$ is a probability distribution (i.e., $p_j \geq 0$ and $\sum_j p_j = 1$) and $\rho_j^{A(B)} \in \mathcal{H}_{A(B)}$ is the reduced density operator of subsystem A (B). States that can be written in the form of (3) are said to be separable. All other states are said to be entangled (or nonseparable).

The above-discussed nonlocal and nonseparable aspects of the correlations in a composite system are distinctive features of the quantum realm. It is tempting to believe that they thoroughly describe the quantum nature of the multipartite state, but a characterization attentive only to entanglement would be incomplete. To construct a more encompassing description, we have to examine the possibility of locally redistributing the correlations. In 2008, Piani and coauthors proved the so-called no-local-broadcasting theorem [10], showing that local operations can redistribute the correlations in a bipartite state ρ_{AB} if and only if the latter can be cast in the following form:

$$\rho_{AB}^{\mathrm{cc}} = \sum_{j,k} p_{jk} |\psi_j^A\rangle\langle\psi_j^A| \otimes |\phi_k^B\rangle\langle\phi_k^B|, \tag{4}$$

where $\{p_{jk}\}$ is a probability distribution and the $\{|\psi_j^A\rangle\}$ ($\{|\phi_k^B\rangle\}$) defines an orthonormal basis for subsystem A (B).

Comparison of (4) with (3) shows that ρ_{AB}^{cc} forms a non convex set that is a subset of the separable states. It follows that quantum correlations, i.e., correlations that cannot be locally broadcast, can be found even in separable states. Nonclassical correlations of this kind can be identified and quantified by the measure we discuss next.

1.2 Quantum Discord

Our review is focused on quantum discord (QD). This quantity stands out among the measures of quantum correlations because it was proposed first and has been most widely studied. Detailed discussions of other quantum correlation measures and their properties have been presented in two recent reviews [16, 17].

Before turning to QD, we find it instructive to briefly review certain aspects of classical information theory, to set the notation and define relevant quantities.

1.2.1 Concepts from Classical Information Theory

In classical information theory, the uncertainty of a random variable A is quantified by its Shannon entropy [11]

$$H(A) := -\sum_a p_a \log_2 p_a, \tag{5}$$

where $p_a := \Pr(A = a)$ stands for the probability that A takes the value a. The binary logarithm expresses information in bits.

Two random variables are said to be correlated if they share information. Knowledge about one of them, say B, yields information about the other, A. The difference in the uncertainties of A before and after we know B,

$$J(A{:}B) := H(A) - H(A|B), \tag{6}$$

a quantity named mutual information, is a measure of the correlation between the two random variables (A and B).

In (6), the conditional entropy reads

$$H(A|B) := -\sum_{a,b} p_{a,b} \log_2 p_{a|b}, \tag{7}$$

where $p_{a,b} := \Pr(A = a, B = b)$.

Given the definition for the conditional probability for A to take the value a when B is equal to b, namely $p_{a|b} := p_{a,b}/p_b$, we have that

$$H(A|B) = H(A,B) - H(B), \tag{8}$$

with $H(A, B) = -\sum_{a,b} p_{a,b} \log_2 p_{a,b}$.

Hence, the following equivalent expression for the mutual information between A and B can be written:

$$I(A{:}B) = H(A) + H(B) - H(A,B). \tag{9}$$

In classical information theory, the relation

$$J(A{:}B) = I(A{:}B) \tag{10}$$

is always valid; the two expressions for the mutual information are equivalent. The same is not true, in general, of the extensions of $J(A{:}B)$ and $I(A{:}B)$ to quantum states. This nonequivalence is at the heart of the definition of quantum discord, which therefore measures the quantum aspects of correlation.

1.2.2 Original Definition of Quantum Discord

The uncertainty about a system S, described by a density operator ρ_S, is quantified in quantum information theory by the von Neumann entropy [12]:

$$S(\rho_S) := -\mathrm{Tr}(\rho_S \log_2 \rho_S). \tag{11}$$

A direct extension of the mutual information in (9) is therefore given by the equality

$$\mathcal{I}(\rho_{AB}) := S(\rho_A) + S(\rho_B) - S(\rho_{AB}). \tag{12}$$

$\mathcal{I}(\rho_{AB})$, named quantum mutual information, can be regarded as a measure of the total correlations between subsystems A and B when the joint system is in the state ρ_{AB} [13, 14].

To extend to the quantum realm, the mutual information in (6), consider the measurement of an observable represented by the following Hermitian operator:

$$O_B = \sum_j o_j |\Pi_j^B\rangle\langle\Pi_j^B|, \tag{13}$$

defined on the state space of subsystem B, $\mathcal{H}_B$.

If the system is initially in the state ρ_{AB}, the value o_j is obtained with probability

$$p_j = \mathrm{Tr}\left(\mathbb{I}_A \otimes \Pi_j^B \rho_{AB}\right) \tag{14}$$

and the state of subsystem A, immediately after the measurement, reads

$$\rho_j^A = \frac{1}{p_j}\mathrm{Tr}_B\left(\mathbb{I}_A \otimes \Pi_j^B \rho_{AB} \mathbb{I}_A \otimes \Pi_j^B\right). \tag{15}$$

In (14) and (15), $\left\{\Pi_j^B\right\}$ is a complete set of von Neumann's measurements on subsystem B satisfying the relations $\sum_j \Pi_j^B = \mathbb{I}_B$ and $\Pi_j^B \Pi_k^B = \delta_{jk}\Pi_j^B$.

The average quantum conditional entropy of subsystem A, given the measurement of the observable O_B on subsystem B, is determined by the expression

$$S(\rho_{A|B}) = \sum_j p_j S\left(\rho_j^A\right). \tag{16}$$

A quantum extension of $J(A{:}B)$ can therefore be defined as follows:

$$\mathcal{J}(\rho_{AB}) := S(\rho_A) - S(\rho_{A|B}). \tag{17}$$

The two expressions for the quantum mutual information, (12) and (17), are in general inequivalent. The difference

$$\mathcal{D}_B(\rho_{AB}) := \mathcal{I}(\rho_{AB}) - \max_{O_B} \mathcal{J}(\rho_{AB}), \tag{18}$$

a measure of quantum correlation in bipartite systems, was named quantum discord [15].

The maximum on the right-hand side of (18) is obtained from the measurements (on subsystem B) providing maximal information about A. An alternative version of QD, $\mathcal{D}_A$, can be obtained from measurements of an observable O_A on subsystem A. In general, $\mathcal{D}_A \neq \mathcal{D}_B$, an asymmetry of QD with several interesting physical interpretations as well as information-theoretical implications [16, 17].

If the mutual information is taken as a measure of total correlations, one can verify that QD may be written as the difference between the mutual informations of the subsystems before and after a complete map of von Neumann's measurements is applied to one of the subsystems:

$$\mathcal{D}_B(\rho_{AB}) = \mathcal{I}(\rho_{AB}) - \max_{\Pi^B} \mathcal{I}\left(\Pi^B(\rho_{AB})\right), \tag{19}$$

where $\Pi^B(\rho_{AB}) = \sum_j (\mathbb{I}_A \otimes \Pi_j^B)\rho_{AB}(\mathbb{I}_A \otimes \Pi_j^B)$.

In this alternative definition, QD can be interpreted as a measure of those correlations that are inevitably destroyed by the measurement.

1.3 Nuclear Magnetic Resonance Systems in Quantum Information Science

We expect the relation between nonclassical correlations and the advantages offered by quantum information science over classical protocols to play an important role in the quest for quantum speedup. Nuclear magnetic resonance (NMR) has been one of the leading experimental platforms for the implementation of protocols and algorithms in QIS [18] and simulation of

quantum systems [19]. NMR implementations encode the qubits in nuclear spins that are manipulated by carefully designed sequences of radio-frequency (rf) pulses. The information about the system state is obtained directly from the transverse magnetizations, the natural NMR observables [37]. The NMR density operator is typically highly mixed. In fact, Braunstein and coauthors showed that no entanglement was generated in most NMR implementations of QIS protocols [20]. In another line of work, Vidal proved that a large amount of entanglement must be generated if a pure-state quantum computation is to provide exponential speedup of information processing [21]. The conjunction of these results led to doubts contrasting the possible classical nature of NMR with the envisioned QIS implementations.

Around the same time, however, it was realized that, while necessary, entanglement generation was not sufficient for gain, even in pure-state quantum computation [22]. In the last decade, it has become progressively clearer that the quantum speedup in the mixed-state quantum computation scenario depends on more subtle components [23–26]. In particular, although a definitive proof is still lacking, QD has been identified as the figure of merit for quantum advantage [27, 28].

Important as this issue is, to settle it is not the goal of this review. We deal only with the theoretical and experimental quantification or identification of quantum correlations in NMR systems at room temperature. We discuss the signatures of quantumness in the correlations of highly mixed NMR states and study the dynamics of the correlations under decoherence.

2 Quantification and Identification of Quantum Correlations

2.1 Symmetric Quantum Discord

As mentioned in Section 1.2.2, the original definition of QD is asymmetric with respect to the subsystem we choose to measure. As an illustration, let us consider the following bipartite state:

$$\rho_{AB}^{\mathrm{cq}} = \sum_i p_i |\psi_i^A\rangle\langle\psi_i^A| \otimes \rho_i^B, \tag{20}$$

where $\{p_i\}$ is a probability distribution, $\{|\psi_i^A\rangle\} \in \mathcal{H}_A$ is an orthonormal basis for subsystem A, and $\rho_i^B \in \mathcal{H}_B$ is the reduced density operator of subsystem B.

In this case, $\mathcal{D}_A(\rho_{AB}^{\mathrm{cq}})$ vanishes, while the alternative definition of QD, $\mathcal{D}_B(\rho_{AB}^{\mathrm{cq}})$, is null if and only if all ρ_i^B commutes, that is, if $[\rho_i^B, \rho_j^B] = 0$ for all i and j. Moreover, numerical calculations indicate that if ρ_{AB} is asymmetric with respect to subsystem interchange or, more specifically, if $S(\rho_A) \neq S(\rho_B)$, then $\mathcal{D}_A(\rho_{AB}) \neq \mathcal{D}_B(\rho_{AB})$ [29]. At first glance, given that the correlations are associated with the information shared between subsystems, this asymmetry may seem surprising. The asymmetry is nonetheless compatible with the sharing, because the quantumness limits differently the amount of information available to observers via local measurements in each subsystem.

Only for the class of states in (4) do we have that $\mathcal{D}_A(\rho_{AB}^{\mathrm{cc}}) = \mathcal{D}_B(\rho_{AB}^{\mathrm{cc}}) = 0$. A quantity that identifies and, to some extent, quantifies the quantumness of correlations in states that cannot be cast in the form of (4) can be defined by the equality [29]

$$\mathcal{D}(\rho_{AB}) := \mathcal{I}(\rho_{AB}) - \max_{\Pi^{AB}} \mathcal{I}\left(\Pi^{AB}(\rho_{AB})\right), \tag{21}$$

where the complete map of local von Neumann measurements reads

$$\Pi^{AB}(\rho_{AB}) := \sum_{j,k} \left(\Pi_j^A \otimes \Pi_k^B\right) \rho_{AB} \left(\Pi_j^A \otimes \Pi_k^B\right), \tag{22}$$

with $\sum_j \Pi_j^s = \mathbb{I}_s$ and $\Pi_j^s \Pi_k^s = \delta_{jk} \Pi_j^s$ for $s = A, B$.

This quantum correlation quantifier can be regarded as a symmetric version of QD. Since the state $\Pi^{AB}(\rho_{AB})$ is classical, we define the classical counterpart of $\mathcal{D}$,

$$\mathcal{C}(\rho_{AB}) := \max_{\Pi^{AB}} \mathcal{I}\left(\Pi^{AB}(\rho_{AB})\right), \tag{23}$$

as a measure of the classical correlations in ρ_{AB}.

2.2 Symmetric Quantum Discord for the Deviation Matrix

We now show how to obtain the classical correlation (23) and the symmetric quantum discord (21) for systems described by density matrices of the form [33]

$$\rho_{AB} = \frac{\mathbb{I}_{AB}}{4} + \epsilon \Delta\rho_{AB}, \tag{24}$$

where $\epsilon \ll 1$ and $\Delta\rho_{AB}$ is a traceless deviation matrix, $\mathrm{Tr}(\Delta\rho_{AB}) = 0$.[1]

In order to calculate the quantum mutual information, we need to compute the von Neumann entropy. To that end, we take advantage of the eigen decomposition of ρ_{AB} to write that

$$\ln(\rho_{AB}) = \sum_j \ln(1/4 + \epsilon\lambda_j) |\lambda_j\rangle\langle\lambda_j|. \tag{25}$$

[1] Equation (24) contains the typical density operator describing the state of NMR systems.

The Taylor expansion of $\ln(1/4+\epsilon\lambda_j)$ then yields

$$\begin{aligned} S(\rho_{AB}) &= -\frac{1}{\ln 2}\mathrm{Tr}(\rho_{AB}\ln\rho_{AB}) \\ &= \mathrm{Tr}\left(\frac{\mathbb{I}_{AB}}{2}+\frac{\epsilon(2\ln 2-1)}{\ln 2}\Delta\rho_{AB}-\frac{2\epsilon^2}{\ln 2}\Delta\rho_{AB}^2+\cdots\right) \\ &= 2-\frac{2\epsilon^2}{\ln 2}\mathrm{Tr}(\Delta\rho_{AB}^2)+\cdots. \end{aligned} \tag{26}$$

Since the reduced density matrices have the form

$$\rho_s = \frac{\mathbb{I}_s}{2}+\epsilon\Delta\rho_s, \tag{27}$$

with $s=A,B$, the same procedure can be used to compute

$$S(\rho_s) = 1-\frac{\epsilon^2}{\ln 2}\mathrm{Tr}\left(\Delta\rho_s^2\right)+\cdots. \tag{28}$$

In view of (26) and (28), we can express the quantum mutual information in terms of the deviation matrix. Up to second order in ϵ, we have that

$$\mathcal{I}(\rho_{AB}) \approx \frac{\epsilon^2}{\ln 2}\left[2\mathrm{Tr}\left(\Delta\rho_{AB}^2\right)-\mathrm{Tr}\left(\Delta\rho_A^2\right)-\mathrm{Tr}\left(\Delta\rho_B^2\right)\right]. \tag{29}$$

The measured state obtained from ρ_{AB} through a complete set of local projective measurements reads

$$\Pi^{AB}(\rho_{AB}) = \frac{\mathbb{I}_{AB}}{4}+\epsilon\Delta\eta_{AB}, \tag{30}$$

with the measured deviation matrix given by the equality

$$\begin{aligned} \Delta\eta_{AB} &:= \Pi^{AB}(\Delta\rho_{AB}) \\ &= \sum_{j,k}\left(\Pi_j^A\otimes\Pi_k^B\right)\Delta\rho_{AB}\left(\Pi_j^A\otimes\Pi_k^B\right) \end{aligned}$$

and $\mathrm{Tr}\left[\Pi^{AB}(\Delta\rho_{AB})\right]=0$.

The procedure leading to (29) now yields the following expression for the mutual information of the measured state:

$$\begin{aligned} \mathcal{I}\left(\Pi^{AB}(\rho_{AB})\right) \approx \frac{\epsilon^2}{\ln 2}\times\big[&2\mathrm{Tr}\left(\Delta\eta_{AB}^2\right)-\mathrm{Tr}\left(\Delta\eta_A^2\right) \\ &-\mathrm{Tr}\left(\Delta\eta_B^2\right)\big], \end{aligned} \tag{31}$$

where $\Delta\eta_{A(B)}=\mathrm{Tr}_{B(A)}(\Delta\eta_{AB})$. The symmetric QD and the classical correlation are then computed from (21) and (23), respectively.

2.3 Symmetric Quantum Discord for Two-Qubit States

Any two-qubit state can be brought, through local unitary transformations, to the following form:

$$\begin{aligned} \rho_{AB} = \frac{1}{4}\Bigg[&\mathbb{I}_{AB}+\sum_{j=1}^{3}\left(a_j\sigma_j^A\otimes\mathbb{I}_B+b_j\mathbb{I}_A\otimes\sigma_j^B\right) \\ &+\sum_{j=1}^{3}c_j\sigma_j^A\otimes\sigma_j^B\Bigg], \end{aligned} \tag{32}$$

where $\{\sigma_j^s\}$ is the Pauli operator acting on $\mathcal{H}_s$ and $a_j, b_j, c_j\in\mathbb{R}$. The measured state, modulo local unitary transformations, can be written in the form

$$\begin{aligned} \Pi^{AB}(\rho_{AB}) = \frac{1}{4}\big(&\mathbb{I}_{AB}+\alpha\sigma_3^A\otimes\mathbb{I}_B+\beta\mathbb{I}_A\otimes\sigma_3^B \\ &+\gamma\sigma_3^A\otimes\sigma_3^B\big), \end{aligned} \tag{33}$$

with

$$\alpha := \sum_j a_j z_j^A,\quad \beta := \sum_j b_j z_j^B,\quad \gamma := \sum_j c_j z_j^A z_j^B. \tag{34}$$

The parameters

$$\begin{aligned} z_1^s &= 2\sin\theta_s\cos\theta_s\cos\phi_s, \\ z_2^s &= 2\sin\theta_s\cos\theta_s\sin\phi_s, \\ z_3^s &= 2\cos^2\theta_s-1, \end{aligned}$$

with

$$\theta_s\in[0,\pi/2]\text{ and }\phi_s\in[0,2\pi], \tag{35}$$

determine the measurement direction for subsystem $s=A,B$.

One might fear that the maximization problem on the right-hand side of (23), associated with the computation of the classical correlation, cannot be solved in general. Nevertheless, for Bell-diagonal states,

$$\rho_{AB}^{\mathrm{bd}} = \frac{1}{4}\left(\mathbb{I}_{AB}+\sum_{j=1}^{3}c_j\sigma_j^A\otimes\sigma_j^B\right), \tag{36}$$

the correlations can be obtained analytically. In this case, we have that $S(\rho_A^{\mathrm{bd}})=S(\rho_B^{\mathrm{bd}})=1$, and (23) becomes

$$C\left(\rho_{AB}^{\mathrm{bd}}\right) = 2-\min_{\gamma}S\left[\Pi^{AB}\left(\rho_{AB}^{\mathrm{bd}}\right)\right], \tag{37}$$

with

$$S\left(\Pi^{AB}\left(\rho_{AB}^{\mathrm{bd}}\right)\right) = -\sum_{j=1}^{4}\frac{1+(-1)^j\gamma}{4}\log_2\frac{1+(-1)^j\gamma}{4}. \tag{38}$$

The minimum of the measured state entropy is obtained by maximizing $|\gamma|$. It results that

$$|\gamma| \leq \kappa := \max(|c_1|, |c_2|, |c_3|). \tag{39}$$

An analytical expression for the symmetric QD for Bell-diagonal states is then obtained [29]:

$$\mathcal{D}(\rho_{AB}^{\mathrm{bd}}) = \sum_{j,k=0}^{1} \lambda_{jk}^{\mathrm{bd}} \log_2 4\lambda_{jk}^{\mathrm{bd}} - \mathcal{C}\left(\rho_{AB}^{\mathrm{bd}}\right), \tag{40}$$

with

$$\mathcal{C}\left(\rho_{AB}^{\mathrm{bd}}\right) = \frac{1}{2}\sum_{j=0}^{1}\left[1+(-1)^j\kappa\right]\log_2\left[1+(-1)^j\kappa\right] \tag{41}$$

and $\lambda_{jk}^{\mathrm{bd}} = [1+(-1)^j c_1 - (-1)^{j+k}c_2 + (-1)^j c_3]/4$.

2.4 Dynamics of Correlations under Decoherence

We shall use the analytical expressions for the symmetric QD (40) and its classical counterpart (41) in Bell-diagonal states to study the dynamics of these correlations under the influence of a local, independent Markovian environments that inject phase noise into the system, as schematically depicted in Fig. 1 [30]. Under such conditions, the two subsystems A and B, initially prepared in a Bell-diagonal state (36), evolve via the following quantum operation [9]:

$$\begin{aligned}\rho_{AB}^{\mathrm{bd}}(p) &= \mathcal{E}_{\mathrm{PD}}\left(\rho_{AB}^{\mathrm{bd}}\right) \\ &= \sum_{j,k}\left(K_j^A \otimes K_k^B\right)\rho_{AB}^{\mathrm{bd}}\left(K_j^A \otimes K_k^B\right)^{\dagger} \qquad (42)\\ &= \frac{1}{4}\begin{bmatrix} 1+\gamma & 0 & 0 & \alpha-\beta \\ 0 & 1-\gamma & \alpha+\beta & 0 \\ 0 & \alpha+\beta & 1-\gamma & 0 \\ \alpha-\beta & 0 & 0 & 1+\gamma \end{bmatrix}. \qquad (43)\end{aligned}$$

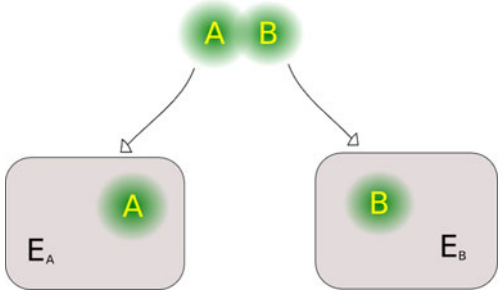

Fig. 1 (Color online) Schematic representation of the two systems A and B, initially prepared in a state ρ_{AB}, evolving under the action of local, independent phase channels

All matrices in this article are represented in the standard computational basis $\{|00\rangle, |01\rangle, |10\rangle, |11\rangle\}$, where $|ij\rangle := |i\rangle \otimes |j\rangle$ and $\{|0\rangle, |1\rangle\}$ are the eigenstates of the Pauli matrix σ_z. The Kraus operators in the operator-sum representation (42) for the phase-damping channel are

$$\begin{aligned} K_0^s &= \sqrt{1-\frac{p_s}{2}}\begin{bmatrix}1 & 0\\ 0 & 1\end{bmatrix}, \\ K_1^s &= \sqrt{\frac{p_s}{2}}\begin{bmatrix}1 & 0\\ 0 & -1\end{bmatrix}, \end{aligned} \tag{44}$$

where $s = A, B$ and $p_A = p_B := p$ is the parametrized time.

We have chosen identical environments for the two subsystems and use the shorthands

$$\begin{aligned}\alpha &:= (1-p)^2 c_1, \\ \beta &:= (1-p)^2 c_2, \\ \gamma &:= c_3.\end{aligned}$$

We can see that the time-evolved density matrix (43) has the Bell-diagonal form (36). Thus, the symmetric QD $\mathcal{D}\left[\rho_{AB}^{\mathrm{bd}}(p)\right]$ and the classical correlation $\mathcal{C}\left[\rho_{AB}^{\mathrm{bd}}(p)\right]$ are given by (40) and (41), respectively, with

$$\kappa = \max(|\alpha|, |\beta|, |\gamma|) \tag{45}$$

and

$$\lambda_{jk}^{\mathrm{bd}} = [1+(-1)^j\alpha - (-1)^{j+k}\beta + (-1)^j\gamma]/4. \tag{46}$$

The analytical results define three classes of behavior for the correlations under decoherence, according to the coefficients c_j $(j = 1, 2, 3)$ in the sum within parentheses on the right-hand side of (36):

(i) If $|c_3| \geq |c_1|, |c_2|$, we have that $\kappa = |c_3|$, which makes the classical correlation independent of the parametrized time p. Since the quantum correlation decays monotonically to zero in the asymptotic-state limit, the classical correlation is equal to the mutual information, i.e.,

$$\mathcal{C}\left[\rho_{AB}^{\mathrm{bd}}(p)\right] = \mathcal{C}\left[\rho_{AB}^{\mathrm{bd}}(p=0)\right] = \mathcal{I}\left[\rho_{AB}^{\mathrm{bd}}(p=1)\right]. \tag{47}$$

Figure 2 shows the evolution of the correlations for an initial state ρ_{AB}^{bd} defined by the parameters $c_1 = 0.06$, $c_2 = 0.3$, and $c_3 = 0.33$, which belong to this class.

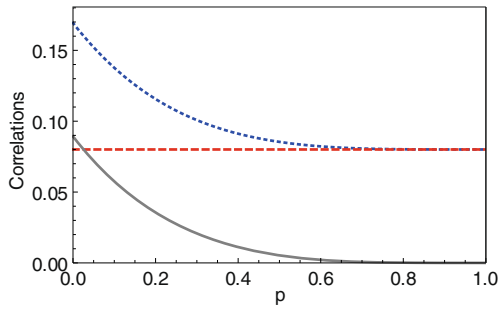

Fig. 2 (Color online) Total correlation (*dotted line, blue online*), classical correlation (*dashed line, red online*), and quantum discord (*black solid line*) for the Bell-diagonal initial state in (36) with the parameters $c_1 = 0.06$, $c_2 = 0.3$, and $c_3 = 0.33$ evolving under local, independent phase-damping channels. Since $|c_3| > |c_1|, |c_2|$, the parametrical set belongs to class (i), defined in the text. The classical correlation is not affected by the environment, while the quantum correlation decays monotonically

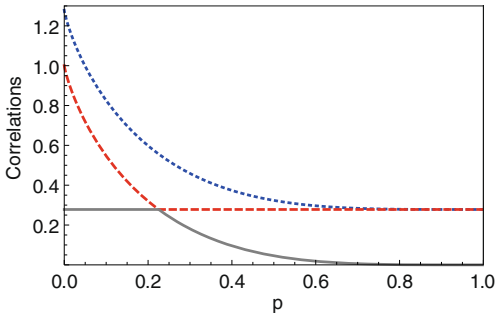

Fig. 3 (Color online) Total correlation (*dotted line, blue online*), classical correlation (*dashed line, red online*), and quantum discord (*black solid line*) for a Bell-diagonal initial state evolving under local, independent phase-damping channels. Analogous to Fig. 2. Here, the initial-state parameters are $c_1 = 1$, $c_2 = -0.6$, and $c_3 = 0.6$, within class (ii). The behaviors of the partial correlations change suddenly at $p = p_{sc} \approx 0.22$. While constant (monotonically decaying) for $p < p_{sc}$, the quantum discord (classical correlation) decays monotonically (remains constant) for $p > p_{sc}$

(ii) If $|c_1| \geq |c_2|, |c_3|$ or $|c_2| \geq |c_1|, |c_3|$, and $|c_3| \neq 0$ the dynamics of the correlations under decoherence exhibits a sudden change at the parametrized time

$$p_{sc} = 1 - \sqrt{\frac{|c_3|}{\max(|c_1|, |c_2|)}}. \tag{48}$$

For $p < p_{sc}$, we have that $\kappa = (1-p)^2 \max(|c_1|, |c_2|)$, so that the classical correlation $\mathcal{C}$ decays monotonically. By contrast, for $p \geq p_{sc}$, we have that $\kappa = |c_3|$ and $\mathcal{C}$ is constant:

$$\mathcal{C}\left[\rho_{AB}^{bd}(p > p_{sc})\right] = \mathcal{I}\left[\rho_{AB}^{bd}(p = 1)\right], \tag{49}$$

while the decay rate of $\mathcal{D}$ changes abruptly at $p = p_{sc}$.

Figure 3 shows an example. The initial state ρ_{AB}^{bd} is now defined by $c_1 = 1$, $c_2 = -0.6$, and $c_3 = 0.6$. In this example, not only does the classical correlation remain constant in a certain time interval, but also the quantum correlation in unaffected by decoherence in another interval. The regimes in which $\mathcal{D}$ = constant and $\mathcal{C}$ = constant were named classical and quantum decoherence regimes, respectively, in [31].

(iii) Finally, if $c_3 = 0$, both correlations $\mathcal{C}$ and $\mathcal{D}$ decay monotonically. Figure 4 shows an example of this kind of behavior, for a Bell-diagonal initial state with $c_1 = c_2 = 0.25$ and $c_3 = 0.0$.

2.5 Witness of Classicality

The set composed by separable states of the form (3) is convex. There is hence a linear Hermitian operator, known as the entanglement witness, that distinguishes separable from entangled states. It is natural to ask whether the same approach can be used to identify classical states. It turns out that the set formed by states with null QD is not convex. As a consequence, linear witnesses can no longer be defined.

To verify this assertion, consider a linear Hermitian operator W_l whose mean value is nonnegative for classical states, i.e.,

$$\langle W_l \rangle_{\rho_{AB}^{cc}} = \mathrm{Tr}(W_l \rho_{AB}^{cc}) \geq 0, \tag{50}$$

while $\langle W_l \rangle_{\rho_{AB}} < 0$ for quantum-correlated states. Since the separable states in (3) satisfy the inequality

$$\langle W_l \rangle_{\rho_{AB}^{sep}} = \sum_j p_j \langle W_l \rangle_{\rho_j^A \otimes \rho_j^B} \geq 0, \tag{51}$$

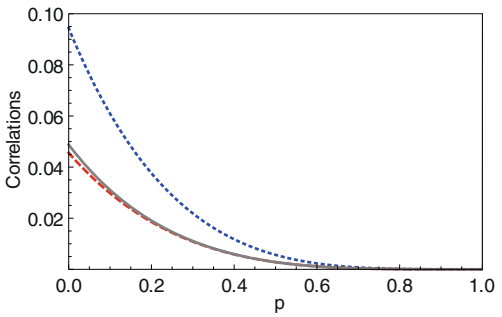

Fig. 4 (Color online) Total correlation (*dotted line, blue online*), classical correlation (*dashed line, red online*), and quantum discord (*black continuous line*) for a Bell-diagonal initial state evolving under local independent phase-damping channels. Analogous to Fig. 2. The initial-state parameters are now $c_1 = c_2 = 0.25$ and $c_3 = 0.0$, within class (iii). All correlations decay monotonously with time

the linear operator W_{ij} cannot identify separable discordant states.

To overcome this difficulty, one introduces a nonlinear classicality witness providing a sufficient condition for the absence of quantumness in the correlations of two-qubit states of the form (32) [32]. To this end, consider the following set of Hermitian operators

$$O_j = \sigma_j^A \otimes \sigma_j^B,$$
$$O_4 = \vec{z}\cdot\vec{\sigma}_A \otimes \mathbb{I}_B + \mathbb{I}_A \otimes \vec{w}\cdot\vec{\sigma}_B,$$

where $j = 1, 2, 3$, and the $\vec{z}, \vec{w} \in \mathbb{R}^3$ $(|\vec{z}| = |\vec{w}| = 1)$ should be randomly chosen. Consider next the following relation among the averages of these operators:

$$W_{\rho_{AB}} = \sum_{i=1}^{3}\sum_{j=1+1}^{4} |\langle O_i\rangle_{\rho_{AB}}\langle O_j\rangle_{\rho_{AB}}|, \tag{52}$$

where $|x|$ is the absolute value of x.

We can see that $W_{\rho_{AB}} = 0$ if and only if the mean values of at least three of the above-defined four observables are zero. Since

$$\langle O_i\rangle_{\rho_{AB}} = c_i \text{ for } i = 1, 2, 3,$$
$$\langle O_4\rangle_{\rho_{AB}} = \vec{z}\cdot\vec{a} + \vec{w}\cdot\vec{b},$$

with $\vec{a} = (a_1, a_2, a_3)$ and $\vec{b} = (b_1, b_2, b_3)$, the only way to insure that $W_{\rho_{AB}} = 0$ is to impose that ρ_{AB} be of the type

$$\chi_i = \frac{1}{4}\left(\mathbb{I}_{AB} + c_i\sigma_i^A \otimes \sigma_i^B\right) \text{ for } i = 1 \text{ or } i = 2 \text{ or } i = 3,$$
$$\chi_4 = \frac{1}{4}\left[\mathbb{I}_{AB} + \sum_{j=1}^{3}\left(a_j\sigma_j^A \otimes \mathbb{I}_B + b_j\mathbb{I}_A \otimes \sigma_j^B\right)\right].$$

All theses states can be cast in the form of (4) and hence possess no quantum correlations. It follows that $W_{\rho_{AB}} = 0$ is a sufficient condition for ρ_{AB} to be classically correlated or to have no correlations at all.

For Bell-diagonal states, $W_{\rho_{AB}} = 0$ is also a necessary condition for the absence of quantum discord. To show this, we note that the classically correlated state ρ_{AB}^{bd} must have the form $(\mathbb{I}_{AB} + c_i\sigma_i^A \otimes \sigma_i^B)/4$ with $i = 1$, $i = 2$, or $i = 3$, which implies that $W_{\rho_{AB}} = 0$.

For the experimental implementation of the classicality witness (52) in the NMR context[2] that will be presented below, it proves useful to rewrite the witness $W_{\rho_{AB}}$ in terms of the qubits magnetizations, which are the natural observables accessed in NMR experiments. We therefore note that

$$\langle O_i\rangle_{\rho_{AB}} = \left\langle \sigma_1^A \otimes \mathbb{I}_B\right\rangle_{\xi_i} \tag{53}$$

with

$$\xi_i = U_{A\to B}\left[R_{n_i}(\theta_i)\rho_{AB}R_{n_i}^{\dagger}(\theta_i)\right]U_{A\to B}, \tag{54}$$

where

$$U_{A\to B} = |0\rangle\langle 0| \otimes \mathbb{I}_B + |1\rangle\langle 1| \otimes \sigma_1^B \tag{55}$$

is the controlled-NOT gate with qubit A as control and $R_{n_i}(\theta_i) = R_{n_i}^A(\theta_i) \otimes R_{n_i}^B(\theta_i)$, where $R_{n_i}^s(\theta_i)$ is a local rotation of qubit $s = A, B$ by an angle θ_i ($\theta_1 = 0, \theta_2 = \theta_3 = \pi/2$) in the direction $\hat{n}_i$ ($\hat{n}_2 = \hat{y}, \hat{n}_3 = \hat{z}$).

3 Quantum Discord in NMR Systems

3.1 Physical System

In order to experimentally follow the dynamics of correlations under decoherence and to implement the classicality witness discussed in Section 2.5, we have to prepare, manipulate, and measure the state of a two-qubit system in the laboratory. In the NMR picture, two-qubit systems can be achieved using samples presenting either two J-coupled nuclear spins-1/2, where J denotes the scalar spin–spin coupling, or one quadrupolar spin-3/2 system, called quadrupolar spin system, for brevity, in a local electric field gradient. Many examples of two dipolar J-coupled spins-1/2 are available: ^{1}H and ^{13}C nuclei in chloroform ($CHCl_3$) or ^{1}H and ^{31}P nuclei in phosphoric acid (H_3PO_4) [18], for instance. The two-qubit quadrupolar systems used so far in quantum information processing (QIP) usually comprise spin-3/2 nuclei in single crystals [38] or in lyotropic liquid crystals [37, 39]. Examples are ^{23}Na and ^{7}Li nuclei in lyotropic liquid crystals based on sodium dodecyl sulfate (SDS) [37] and lithium tetrafluoroborate ($LiBF_4$) [39], as well as ^{23}Na in sodium nitrate ($NaNO_3$) single crystals [38].

All of these are equally good representations of two-qubit systems. The nuclear spin interactions driving their quantum evolution being nonetheless distinct, different state preparation, manipulation, and readout techniques are required. Besides, the characteristics of each spin interaction lead to unique features in the decoherence behavior. For these reasons, each system deserves separate discussion.

[2] A modified version of this classicality witness was implemented in the optical context [36].

3.1.1 Two-Dipolar J-Coupled Nuclear Spin-1/2 System—Liquid Sample

Figure 5 schematically depicts a ^{13}C-enriched chloroform molecule ($CHCl_3$). As already mentioned, the two qubits are constituted by the nuclear ^{1}H $-^{13}$ C spin pair in the molecule. To generate adequate signal strength, many replicas of the two-qubit unit are needed, i.e., an ensemble of spin pairs is required, each spin interacting only with its counterpart in the pair. This is achieved by diluting the ^{13}C-enriched $CHCl_3$ molecules in a deuterated solvent. Since the deuteration and the low natural abundance of ^{13}C make the solvent molecules magnetically inert, from the NMR viewpoint, the system is well described as an ensemble of isolated spin pairs, i.e., numerous replicas of the two-qubit unit.

The results discussed in this section were obtained from a sample prepared by dissolving 100 mg of 99 % ^{13}C-labeled $CHCl_3$ in 0.2 ml of 99.8 % acetone-d_6 and placing this in a 5-mm Wildmad LabGlass tube. Both samples were provided by the Cambridge Isotope Laboratories, Inc. NMR experiments were performed at 25 °C using a 500-MHz Varian Spectrometer and a 5-mm double-resonance probe tuned to the ^{1}H and ^{13}C nuclei.

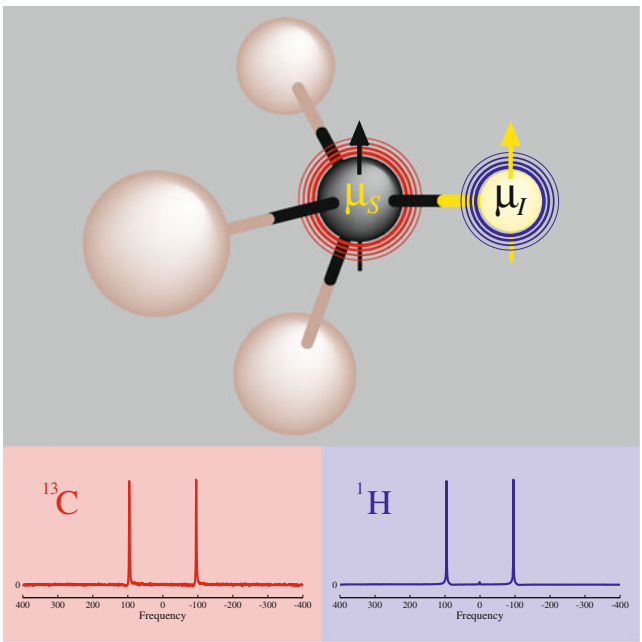

Fig. 5 (Color online) *Top panel*: Schematic representation of chloroform molecule ($HCCl_3$). The halo around the *central* (*left-hand*) sphere depicts perturbation and response of the carbon (hydrogen) nucleus at its respective resonance frequency. *Bottom*: Normalized equilibrium spectra of carbon (*left*) and hydrogen (*right*) nuclei

In NMR experiments, the nuclear spins are placed in a strong static magnetic field $\vec{B}_0$, whose direction defines the positive z-axis. The spins are manipulated by time-dependent rf fields applied to both spins, which interact with each other and their local environments. In a doubly rotating frame with rf frequencies $\omega_{\rm rf}^{\rm H}$ and $\omega_{\rm rf}^{\rm C}$, the Hamiltonian of the two coupled spins reads

$$\begin{aligned}\mathcal{H} = &-\left(\omega_{\rm H}-\omega_{\rm rf}^{\rm H}\right)\mathbf{I}_z^{\rm H}-\left(\omega_{\rm C}-\omega_{\rm rf}^{\rm C}\right)\mathbf{I}_z^{\rm C}+2\pi J\mathbf{I}_z^{\rm H}\mathbf{I}_z^{\rm C}\\ &+\omega_1^{\rm H}\left(\mathbf{I}_x^{\rm H}\cos\varphi^{\rm H}+\mathbf{I}_y^{\rm H}\sin\varphi^{\rm H}\right)\\ &+\omega_1^{\rm C}\left(\mathbf{I}_x^{\rm C}\cos\varphi^{\rm C}+\mathbf{I}_y^{\rm C}\sin\varphi^{\rm C}\right)+\mathcal{H}_{\rm Env}(t),\end{aligned} \tag{56}$$

where $\mathbf{I}_u^{\rm H}$ $(\mathbf{I}_v^{\rm C})$ is the spin angular momentum operator in the $u, v = x, y, z$ direction for ^{1}H (^{13}C) and the angle $\varphi^{\rm H}$ $(\varphi^{\rm C})$ and frequency $\omega_1^{\rm H}$ $(\omega_1^{\rm C})$ define the phase and power, respectively, of the rf field driving the ^{1}H (^{13}C) nuclei.

The first two terms on the right-hand side describe the free precession of ^{1}H and ^{13}C nuclei around $\vec{B}_0$, with Larmor frequencies

$$\frac{\omega_{\rm H}}{2\pi}\approx 500\ \text{MHz and}\ \frac{\omega_{\rm C}}{2\pi}\approx 125\ \text{MHz}. \tag{57}$$

The third term describes the scalar spin–spin coupling (also referred to as J coupling in the NMR literature), converted to the frequency unit:

$$J\approx 215.1\ \text{Hz}. \tag{58}$$

The fourth and fifth terms are the external rf fields applied to manipulate the ^{1}H and ^{13}C nuclear spins, respectively. Finally, $\mathcal{H}_{\rm Env}(t)$ represents time-dependent fields resulting from the random fluctuating in the interactions between the spins and their environment. This term, which includes interactions with the chlorine nuclei and higher order spin–spin couplings, leads to spin relaxation and decoherence.

The density operator for any quantum system in contact with a thermal bath can be written in the form

$$\rho=\frac{\exp(-\beta\mathcal{H})}{\text{Tr}\exp(-\beta\mathcal{H})}, \tag{59}$$

where $\beta = 1/k_BT$.

For two-qubit NMR systems at room temperature, the thermal energy dwarves the magnetic energy:

$$\varepsilon=\frac{\hbar\gamma B_0}{4k_BT}\approx 10^{-5}, \tag{60}$$

where γ is the gyromagnetic ratio.

We can therefore write the density operator in the so-called high-temperature expansion

$$\rho \approx \frac{\mathbb{I}^{ab}}{4} + \varepsilon \Delta\rho, \tag{61}$$

where $\Delta\rho$ is the deviation matrix, the part of the system density matrix that can be manipulated (via rf pulses) and accessed in NMR experiments.

Two unitary transformations are common in NMR experiments: rf pulses and free evolutions of the spin systems under the coupling and static fields. The rf pulses are characterized by intrinsic parameters: amplitude (power), duration, frequency, and phase. Proper setting of these parameters induces nuclear spin rotations about any axis by any rotation angle. For example, a nonselective ^{1}H spin rotation (a hard pulse, in NMR jargon) of $\pi/2$ is the result of a 7.4-μs rf pulse, from which we acquire the ^{1}H equilibrium spectrum (i.e., the NMR spectrum resulting from rf pulses applied to the thermal equilibrium state) shown by the bottom-right panel in Fig. 5. Another simple example is the precession of the nuclear spins around $\vec{B}_0$ in free evolution.

3.1.2 Nuclear Quadrupolar System—Liquid Crystal Sample

We have already mentioned that ^{23}Na ($I = 3/2$) in a SDS molecule of a lyotropic liquid crystal represents a two-qubit quadrupolar spin system well. As depicted in Fig. 6, the ^{23}Na nucleus in this molecule is far from other NMR-active highly abundant nuclei, which are mostly ^{1}H. The magnetic dipolar interaction between ^{23}Na and the other nuclei in the SDS molecule can therefore be neglected. The liquid crystal is moreover prepared with heavy water (D_2O), to weaken the dipolar interaction with the ^{1}H nuclear spins of water, since deuterium has a small gyromagnetic ratio. Therefore, to a good approximation, in the SDS D_2O-based liquid crystal, the interaction between the ^{23}Na quadrupole moment and the electric field gradient produced by the electrical charges in its vicinity (usually called quadrupolar coupling) is the only internal spin interaction affecting the evolution of the quantum system.

The local electric field gradient is defined by the charge configuration in the vicinity of the ^{23}Na nucleus. It follows that, to replicate the ^{23}Na environment throughout the sample, all SDS molecules must have the same orientation. Fortunately, the strong static magnetic field in NMR experiments induces the alignment of the SDS molecules in the lyotropic liquid crystal, naturally leading to the same local electric field gradient at each ^{23}Na site. Furthermore, the anisotropic internal motions of the SDS molecules reduces the strength of the quadrupolar coupling, facilitating the manipulation of the spin system by rf pulses. Under these conditions, in a rotating frame with frequency $\omega_{\rm rf}$, the ^{23}Na nuclear spin Hamiltonian can be described by the expression

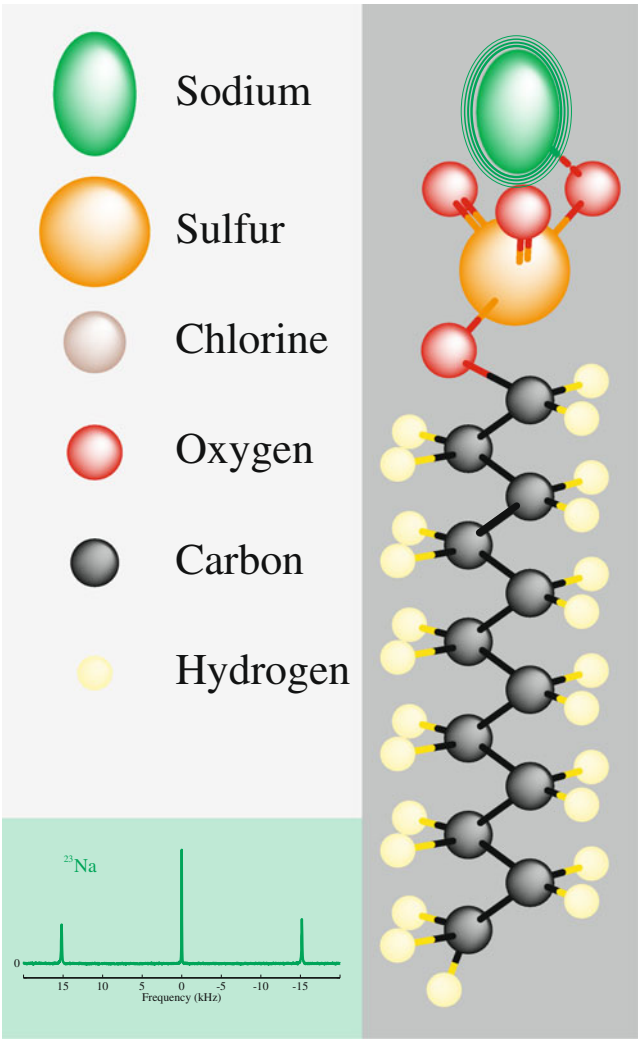

Fig. 6 (Color online) *Top left*: Labels of the atomic components of the molecules. *Bottom left*: Normalized equilibrium spectrum of the sodium nucleus. *Right*: Cartoon representing the sodium dodecyl sulfate molecule (SDS). The *elliptical halo* around the top atom represents the perturbation and response of sodium nucleus at its resonance frequencies

$$\mathcal{H} = -(\omega_{\rm L} - \omega_{\rm rf})\,\mathbf{I}_z + \frac{\omega_{\rm Q}}{6}\left(3\mathbf{I}_z^2 - \mathbf{I}^2\right) + \omega_1\left(\mathbf{I}_x\cos\varphi + \mathbf{I}_y\sin\varphi\right) + \mathcal{H}_{\rm Env}^{\rm Q}(t), \tag{62}$$

where $\omega_{\rm Q}$ is the strength of the quadrupolar coupling expressed in the frequency unit and $\omega_{\rm L}$ is the Larmor frequency ($|\omega_{\rm L}| \gg |\omega_{\rm Q}|$). The spin angular momentum

operator is represented by its u-component $\mathbf{I}_u$ ($u = x, y, z$) and square modulus $\mathbf{I}^2$. The first term on the right-hand side of (62) describes the Zeeman interaction between the static magnetic field and nuclear spin, while the second term accounts for the static first-order quadrupolar interaction. As in (56), the next-to-last and last terms correspond to an externally applied rf field and the time-dependent coupling of the ^{23}Na nuclear spin with its environment, respectively. The latter is mainly due to the motion-induced fluctuations in the local electric field gradients, with smaller contributions from the weak dipolar interactions between the ^{23}Na nucleus and other nearby NMR-active spins [40, 42].

The following experimental results were obtained from a liquid crystal sample prepared with 20.9 % of SDS (95 % of purity), 3.7 % of decanol, and 75.4 % deuterium oxide, following the procedure described in [43]. The ^{23}Na NMR experiments were performed in a 400-MHz Varian Inova spectrometer with a 7 mm solid-state NMR probe head at 26° C. The bottom-left panel in Fig. 6 shows the ^{23}Na equilibrium spectrum of our SDS liquid-crystal sample. The quadrupole coupling frequency is obtained directly from the separation between the central and the satellite lines [44, 45], which yields

$$\nu_{\mathrm{Q}} = \frac{\omega_{\mathrm{Q}}}{2\pi} = 15\ \mathrm{kHz}. \tag{63}$$

Having overviewed the general features of the two main two-qubit NMR systems, we now to turn to their applications in QIP and start out with descriptions of the three central QIP steps, state preparation, manipulation, and readout, in Sections 3.2, 3.3, and 3.4, respectively

3.2 State Preparation

Most of the NMR QIP implementations rely on effectively pure states, usually referred to as pseudo-pure states. Among other methods [46–48], the main procedures for pseudo-pure state preparation are the so-called spatial [47] and temporal averagings [46], which we discuss in this section.

Spatial averaging starts with a system in thermal equilibrium. A set of rf and magnetic field gradient pulses are applied to manipulate the spin populations and coherences (i.e., the diagonal and off-diagonal elements of the density matrix in the computational basis, respectively) and ultimately construct the desired quantum state.

While the rf pulses impose specific spin rotations that change the density matrix populations and coherences, the field gradients eliminate undesired coherences. The gradient pulses generate magnetic field distributions that randomize the phases of the individual quantum coherences and average out their contribution to the final state.

As an example, consider the preparation of the quantum state $|11\rangle$ in the computational basis, which is accomplished by the following pulse sequence, applied to the thermal equilibrium state:

$$\left(\tfrac{\pi}{2}\right)_{-x}^{H,C} \rightarrow \left(\tfrac{1}{4J}\right) \rightarrow \left(\tfrac{\pi}{2}\right)_{y}^{H,C} \rightarrow \left(\tfrac{1}{4J}\right) \rightarrow \left(\tfrac{\pi}{2}\right)_{-x}^{H,C} \rightarrow$$

$$\{G_z\} \rightarrow \left(\tfrac{\pi}{4}\right)_{-y}^{H,C} \rightarrow \left(\tfrac{1}{2J}\right) \rightarrow \left(\tfrac{\pi}{6}\right)_{x}^{H,C} \rightarrow \{G_z\},$$

where $(\theta)_d^{H,C}$ denotes simultaneous rotations of the ^{1}H and ^{13}C nuclear spins by the angle θ around the d-direction, while $(1/nJ)$ indicates the duration of a free evolution and $\{G_z\}$ represents a magnetic field gradient in the z-direction. In practice, each rotation is implemented by a hard rf pulses with appropriate phase (subindex) and amplitude (rotation angle between parentheses), applied to ^{1}H and ^{13}C (superindex) nuclear spins.

Figure 7 compares a numerical simulation of the pulse sequence (rf pulses, free evolutions, and magnetic field gradients) to prepare the state $|11\rangle$ with the experimental procedure. The real and the imaginary parts of the computed (measured) deviation matrix are displayed in the bar plots on the left (right) panels. The experimental deviation matrix was obtained by the quantum state tomography procedure described in Section 3.3.

State preparation by spatial averaging can equally well be achieved by replacing the hard rf pulses and free evolutions by numerically optimized low-power pulses (soft pulses, in NMR terminology) followed by magnetic gradient pulses. Given the excellent experimental control over the NMR variables, the system evolution is accurately described by NMR Hamiltonians defined by the parameters of the rf pulses (the power ω_1, duration t, and phase φ). One can therefore let numerical optimization routines seek the set of pulses that will drive the system from thermal equilibrium to a state such that the diagonal elements of its deviation matrix coincide with those of the target-state deviation matrix. Subsequently, the field-gradient pulse averages out the off-diagonal deviation matrix elements and yields the desired state. Two numerical procedures, named gradient ascent pulse engineering (GRAPE) [49, 50] and strongly modulated pulses (SMP) [51], are commonly used for pulse optimization.

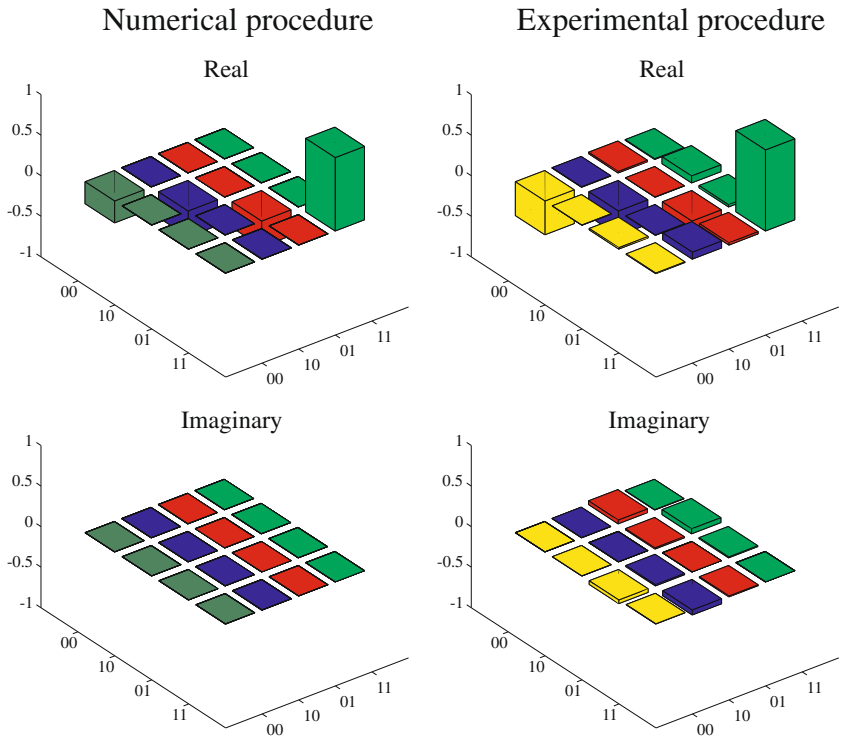

Fig. 7 (Color online) Bar representation of the prepared deviation matrix. The states were generated by hard pulses, free evolutions, and magnetic field gradients. The *top* (*bottom*) part of the figure corresponds to the real (imaginary) part of the deviation matrix. The *left* (*right*) panels correspond to the simulated (experimental) results for the prepared initial quantum state

An example of a SMP pulse sequence implementing a specific initial quantum state is presented in Table 1. The first column indicates the order of application for a certain set of parameters. The second (fifth) and third (sixth) columns show the power and phase of the rf pulses applied to the ^{1}H (^{13}C) nuclei. The fourth column shows the duration of each rf pulse. As already mentioned, a magnetic field gradient is applied after the rf pulses, to wash out the off-diagonal coherences in the deviation matrix.

Table 1 Power, duration, and phase of the rf pulses implementing the SMP technique for the preparation of a predefined quantum state

SMP pulse step	Parameters				
	Hydrogen		Time (ms)	Carbon	
	ω_1^H	φ^H		ω_1^C	φ^C
1	1,092.6	5.94	0.518	1,962.9	1.88
2	1,679.8	5.73	1.546	1,276.7	5.26
3	112.0	1.64	0.226	619.3	2.55
4	1,998.0	2.63	1.130	868.9	3.91
5	211.3	4.84	1.996	835.8	5.46

As explained in the text, the SMP technique is one of the methods that generates quantum states suitable for the NMR study of quantum discord. Of particular interest is the generation of diagonal initial quantum states, as illustrated by the example in Fig. 11. The tabulated parameters define an rf pulse sequence that yields a Bell-diagonal state satisfying the inequality $|c_1|, |c_2| \geq |c_3|$. Similar procedures were followed to obtain other states of interest

The application of the pulse sequence in Table 1 to the thermal equilibrium state, followed by the gradient pulse, was numerically simulated. The resulting real and imaginary parts of the deviation matrix are shown in the left part of Fig. 8. For comparison, the right-hand panels show the deviation matrix measured by quantum state tomography in an experiment using the parameters in the table.

The main advantage of applying SMP or GRAPE pulses followed by magnetic field gradient pulses for state preparation via spatial averaging is versatility. The two techniques yield pulses optimized to produce any desired spin population and are hence more general than the application of hard pulses, which calls for a specific pulse sequence for each desired state.

The preparation of a quantum state via temporal averaging requires a specific number of time-uncorrelated experiments. Each experiment is designed so that the desired state results from the sum of the outcomes of all the experiments. As in spatial averaging, two approaches have been developed: one based on hard pulses [46] and the other based on soft pulses [38, 51]. Time averaging has advantages. In particular, it can generate nondiagonal states, which can be prepared directly from thermal equilibrium since no magnetic gradient pulses are applied.

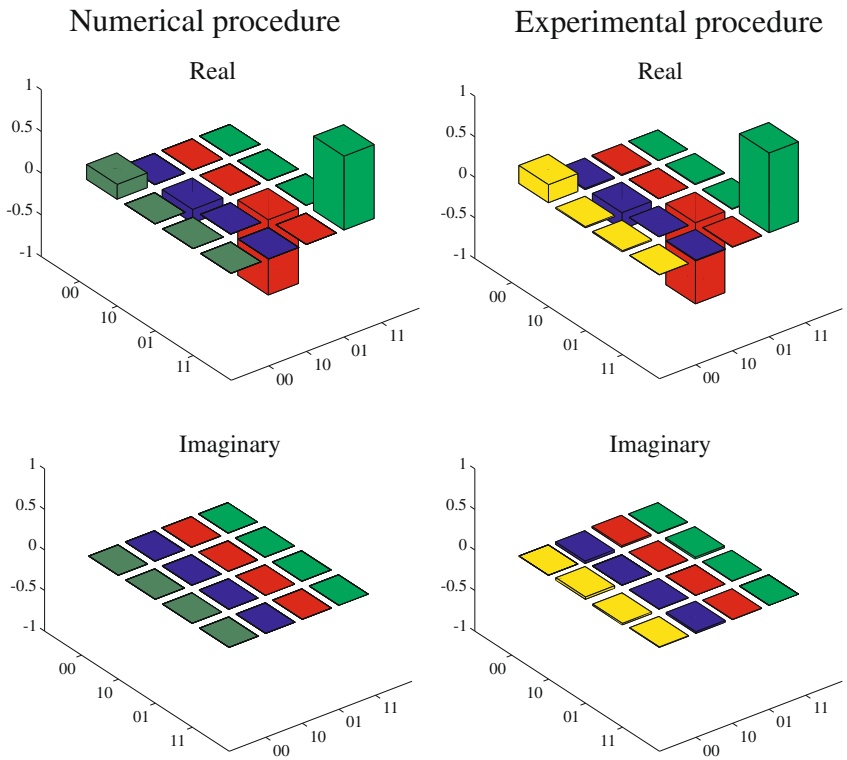

Fig. 8 (Color online) Bar representation of the prepared deviation matrix, obtained from states produced by the SMP technique with the parameters in Table 1. The panels are arranged as in Fig. 7

Figure 9 shows an example of a state prepared by temporal averaging. This state was implemented using ^{23}Na quadrupolar nuclei (spin 3/2) in a lyotropic liquid crystal sample as described in Section 3.1.2. A SMP pulse was also applied to prepare the state, but in this case, the parameters were optimized on the basis of the Hamiltonian (62). Different experiments are labeled by the capital letters A, B, C, and D, each with the five sets of rf pulse parameters (ω_1, t and φ) in Table 2. Each pulse was applied separately to the thermal equilibrium state, resulting in transformed deviation matrices whose sum is the final $\Delta\rho$. The simulated final $\Delta\rho$ is shown by the bar plots in the left panels of Fig. 9. The experimental $\Delta\rho$ is shown by plots in the right panels.

3.3 Quantum State Tomography

Quantum state tomography (QST) uses the observables of a quantum system to measure each element of the corresponding density matrix. In NMR, the observables are the spin magnetizations, which depend on combinations of the density matrix elements corresponding to single quantum transitions ($\Delta m = \pm 1$). Therefore, only those elements located at certain reading positions in the density matrix are readily accessible via experiment.

To determine the other elements, special sequences of rotations must be applied to bring the desired elements to the reading positions in a controlled fashion. After the rotations, the spin magnetizations become dependent on these "nondirectly detectable" elements; proper data processing is then sufficient to determine the latter. The art of finding the minimum number of rotations that allows mapping of the full system density matrix, or the deviation matrix, in the context of NMR, has led to a variety of QST procedures.

Among other sequences in the NMR QIP literature, we find combined spin rotations [53, 54], global spin-system rotations [52], and transition-selective excitations [38, 41]. Generally speaking, each spin system is best served by a specific QST method. For example, while sets of single-spin rotations are more suitable for spin-1/2 systems, transition-selective pulses or global spin rotations are more appropriate for quadrupolar nuclei.

As an illustration, we will briefly discuss the QST technique introduced by Long *et al.* [53]. Widely used for QST of two-coupled spin-1/2 systems, this method has more recently been adapted to systems with more spins [54, 55]. The original version is depicted in Fig. 10. Two sequences of nine spectra running along the left and the right borders of the figure represent the QST procedure, a pair of horizontally aligned spectra corresponding to each of the nine steps in the procedure. Before each step, the system has to be prepared in

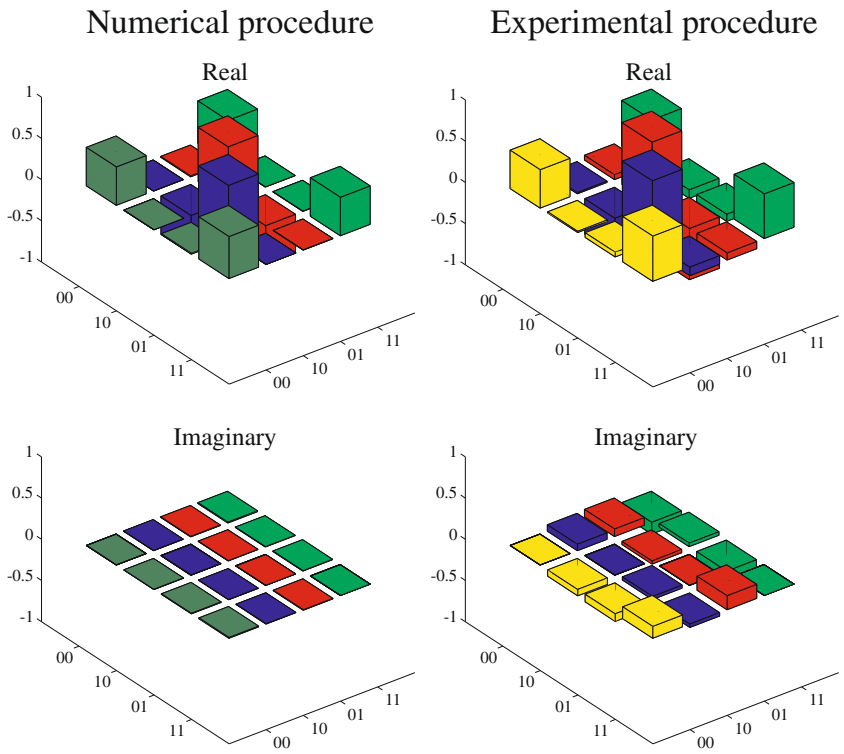

Fig. 9 (Color online) Bar representation of the prepared deviation matrix. The panels are arranged as in Fig. 7. The quantum states were produced by hard pulses, free evolutions, and magnetic field gradients, with the parameters in Table 2

the same state, the deviation matrix of which must be characterized.

In the first step, the NMR signal, i.e., the free induction decay (FID), of both nuclei is acquired, in the absence of rf pulses. The line intensities in the Fourier-transformed FID are recorded, which are represented by the top spectra (labeled **II**) in Fig. 10. In each of the subsequent steps, rf pulses with the phases specified in Table 3 are applied to each or to both nuclei, and the same reading procedure is carried out.

Each plot along the sequence on the left-hand (right-hand) side of Fig. 10 represents the carbon (hydrogen) spectra resulting from each tomography step, carried out after a Bell-diagonal state is prepared in the $CHCl_3$ two-qubit spin system. The spectra are labeled **II**, **XX**, **IX**, **IY**, **XI**, **YI**, **XY**, **YX**, **YY**, to indicate no pulse (**I**), a $\pi/2$ pulse in the positive x-direction (**X**) or a $\pi/2$ pulse in the positive y-direction (**Y**). In the case under study, each spectrum has two spectral lines, each of which has a real and an imaginary component. Altogether, 72 line intensities are therefore recorded.

Each intensity is associated with one or more elements of the deviation matrix. Therefore, to obtain the full deviation matrix, we have to relate the line intensities, i.e., the NMR readouts, to the deviation matrix elements. The rf pulse phases on Table 3 are designed to give access to all elements, with some redundancy to minimize the error.

To be more specific, let us consider the following deviation matrix:

$$\Delta\rho = \begin{bmatrix} a_1 & a_2 + ia_{11} & a_3 + ia_{12} & a_4 + ia_{13} \\ a_2 - ia_{11} & a_5 & a_6 + ia_{14} & a_7 + ia_{15} \\ a_3 - ia_{12} & a_6 - ia_{14} & a_8 & a_9 + ia_{16} \\ a_4 - ia_{13} & a_7 - ia_{15} & a_9 - ia_{16} & a_{10} \end{bmatrix}, \tag{64}$$

containing 16 unknowns.

The rotation imposed on the spins by the rf pulses in step n of the tomographic process can be represented by the operator $\mathbf{U_n}(\mathbf{X}, \mathbf{Y})$. For specified pulse duration and phase, the analytical form of $\mathbf{U_n}(\mathbf{X}, \mathbf{Y})$ is known. Hence, after the nth rotation, the transformed deviation matrix is determined by the expression

$$\Delta\rho_n = \mathbf{U}_n(\mathbf{X}, \mathbf{Y})\, \Delta\rho \mathbf{U}_n^{\dagger}(\mathbf{X}, \mathbf{Y}). \tag{65}$$

After the nth transformation, the real (M_x) and imaginary (M_y) parts of the NMR magnetization for each nuclear spin $\{A, B\}$ are therefore given by the equalities

$$M^A_{x,y;n} = \mathrm{Tr}\left[\Delta\rho_n \left(\mathbf{I}_{x,y} \otimes \mathbb{I}\right)\right]; \tag{66a}$$

$$M^B_{x,y;n} = \mathrm{Tr}\left[\Delta\rho_n \left(\mathbb{I} \otimes \mathbf{I}_{x,y}\right)\right]. \tag{66b}$$

Table 2 Power, duration, and phase of the rf pulses used to prepare quantum states by the SMP technique and the time-averaging procedure

Group set	SMP pulse step	Parameters of sodium nuclei		
		ω_1	φ	Time (μs)
A	1	37,485.4	6.208	15.11
	2	11,624.8	4.243	36.53
	3	31,867.5	3.293	4.15
	4	38,906.5	6.027	47.99
	5	38,681.0	1.927	31.62
B	1	12,063.7	3.919	7.95
	2	15,399.8	3.581	33.74
	3	38,721.2	5.845	30.47
	4	24,148.3	5.117	3.38
	5	38,916.9	3.762	48.08
C	1	39,208.2	1.788	38.82
	2	7,589.9	4.984	27.38
	3	19,817.7	0.889	9.27
	4	38,915.2	1.682	25.45
	5	38,755.6	1.200	21.98
D	1	13,372.2	4.333	15.24
	2	2,192.1	1.506	37.89
	3	39,094.7	4.433	29.35
	4	11,495.7	3.294	10.49
	5	18,867.5	0.213	36.92

The pulse sequences generate the diagonal initial quantum state, as illustrated by the example in Fig. 11. The quantum states resulting from the listed parameters satisfy the inequality $|c_1| \geq |c_2|, |c_3| \neq 0$

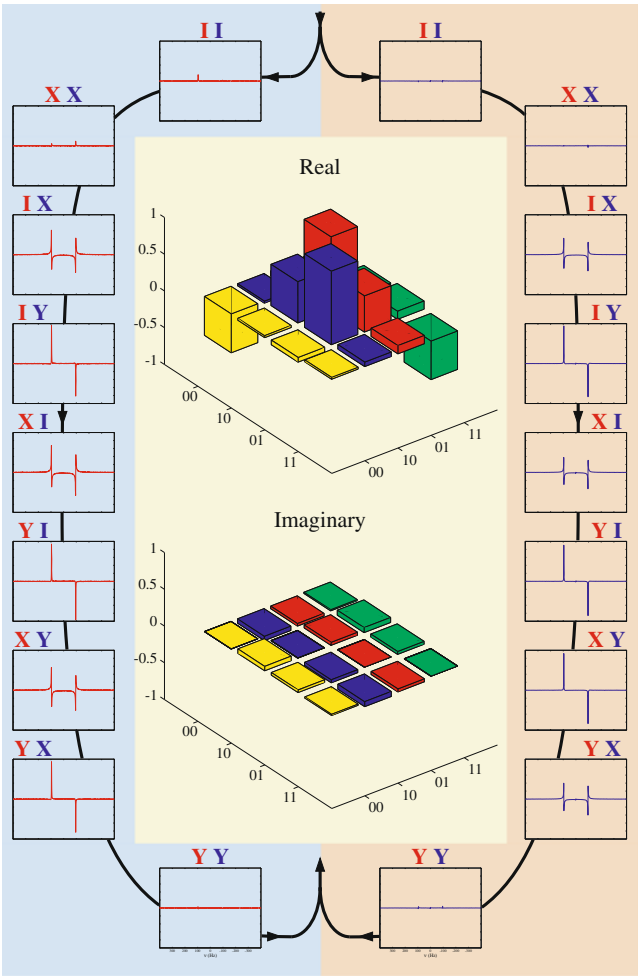

Fig. 10 (Color online) *Outer panels*: NMR spectra of a two-spin system encoded in the chloroform molecule. The spectra are generated by the QST pulse sequence in Table 3. The spectra in the sequence running along the *left-hand* (*right-hand*) border corresponds to the carbon (hydrogen) nuclear spin. *Central panels*: Bar plots representing the real (*top*) and imaginary (*bottom*) parts of the experimental deviation matrix resulting from the QST

Equation (66) linearly relate the magnetizations to the elements of $\Delta\rho$. In other words, for each n, (66a) and (66b) yield two equations of a linear system in which the elements of $\Delta\rho$ are the independent variables, the magnetizations $M^{A,B}_{x,y;n}$ are dependent variables, and the elements of the operators $\mathbf{U_n}(\mathbf{X}, \mathbf{Y})$ are coefficients.

The magnetizations are directly related to the line intensities and hence experimentally accessible, and the $\mathbf{U_n}(\mathbf{X}, \mathbf{Y})$ elements are analytically determined by the rf pulse parameters. Equation (66) is therefore equivalent to the linear system

$$b_k = X_{kj} a_j, \tag{67}$$

where b_k ($k = 1, \ldots, 73$) is the kth recorded line intensity, the a_j ($j = 1, \ldots, 16$) are linearly related by (64) to the $\Delta\rho$ elements before the transformation, and the elements X_{kj} are obtained from the pulse parameters in each QST step.

We solve (67) for a_j to reconstruct the deviation matrix $\Delta\rho$. The bar plots in Fig. 10 show an example.

Table 3 Ordered pulse sequence applied simultaneously to two nuclear species

Pulse order	Carbon	Hydrogen
1st	**I**	**I**
2nd	**X**	**X**
3rd	**I**	**X**
4th	**I**	**Y**
5th	**X**	**I**
6th	**Y**	**I**
7th	**X**	**Y**
8th	**Y**	**X**
9th	**Y**	**Y**

$\mathbf{X} \equiv \left(\frac{\pi}{2}\right)_{+x}$ represents an rf pulse of $\pi/2$ in the positive x-direction. $\mathbf{Y} \equiv \left(\frac{\pi}{2}\right)_{+y}$ represents an rf pulse of $\pi/2$ in the positive y-direction. **I** indicates the absence of rf pulses

The QST methods for quadrupolar nuclei are analogous. Sequences of readouts are obtained after specifically designed rf pulses are applied, the line intensities are recorded, and a linear system is solved to yield the deviation matrix elements. For details, which will not be presented here because they are somewhat more intricate see [52].

3.4 Measurements of Quantum Correlations in NMR Systems

We now discuss the experimental efforts to quantify and identify quantum correlations in NMR systems at room temperature. First, we verify that the peculiar dynamics of quantum discord under decoherence, theoretically predicted for phase-noise channels [30], can occur even under the additional influence of a thermal source [34]. Next, we review the first experimental implementation of a classicality witness [32], which identifies the nature of the correlations in NMR systems even without full QST [35].

3.4.1 Experimental Dynamics of Correlations

Here, we discuss an experimental verification of the sudden change in the quantum discord under decoherence theoretically discussed in Section 2.4. While that effect can in principle be observed in the quadrupolar system described in Section 3.1.2 [33], in practice, serious difficulties arise. In the quadrupolar system, the phase-noise environment is global [56], and the transversal relaxation time, very short.

The transverse relaxation times in the system discussed in Section 3.1.1 are much longer. For this reason, to experimentally demonstrate the peculiar behavior of correlations under decoherence, the two-qubit system encoded in the ^{1}H and ^{13}C nuclear spins of a $CHCl_3$ molecule was used. As already mentioned, relaxation process causing phase decoherence and energy dissipation in this system is mainly due to internal molecular or atomic motions. As a result, the electromagnetic field in which the qubits are immersed fluctuates randomly. To model the resulting decoherence, we combine a phase-damping channel with a generalized amplitude-damping channel, i.e., describe the quantum state by the expression

$$\rho_{AB}(t) = \mathcal{E}_p \circ \mathcal{E}_a(\rho_{AB}), \tag{68}$$

where the quantum operations $\mathcal{E}_n$ $(n = p, a)$ are written in the operator-sum representation as discussed in Section 1, i.e.,

$$\mathcal{E}_n(\rho) = \sum_j K_j^n(t)\rho\left[K_j^n(t)\right]^\dagger. \tag{69}$$

where $K_j^n(t)$ is the Kraus operator.

For the *generalized amplitude-damping* channel, the Kraus operators take the form

$$K_0^a = \sqrt{\gamma}\begin{pmatrix}1 & 0\\ 0 & \sqrt{1-p}\end{pmatrix}, \quad K_1^a = \sqrt{\gamma}\begin{pmatrix}0 & \sqrt{p}\\ 0 & 0\end{pmatrix},$$
$$K_2^a = \sqrt{1-\gamma}\begin{pmatrix}\sqrt{1-p} & 0\\ 0 & 1\end{pmatrix}, \quad K_3^a = \sqrt{1-\gamma}\begin{pmatrix}0 & 0\\ \sqrt{p} & 0\end{pmatrix}, \tag{70}$$

where, in the NMR context,

$$\gamma \approx \frac{1-\varepsilon}{2} \tag{71}$$

and

$$p = 1 - \exp\left(-t/T_1\right). \tag{72}$$

Here, T_1 is the longitudinal relaxation time of the qubit under consideration.

In our case, each qubit has a distinct Larmor frequency and distinct relaxation times. The measured spin–lattice relaxation times are

$$T_1\left(^1\mathrm{H}\right) = 2.5\,\mathrm{s} \quad \text{and} \quad T_1\left(^{13}\mathrm{C}\right) = 7\,\mathrm{s}. \tag{73}$$

The Kraus operators for the *phase-damping* channel are given by (44) with $p = 1 - \exp\left(-t/T_2\right)$, where the measured transverse relaxation times associated with the two qubits are

$$T_2\left(^1\mathrm{H}\right) = 1.8\,\mathrm{s} \quad \text{and} \quad T_2\left(^{13}\mathrm{C}\right) = 0.29\,\mathrm{s}. \tag{74}$$

Since no refocusing pulse was used, the effective transverse relaxation times are

$$T_2^*\left(^1\mathrm{H}\right) = 0.31\,\mathrm{s} \quad \text{and} \quad T_2^*\left(^{13}\mathrm{C}\right) = 0.12\,\mathrm{s}. \tag{75}$$

To attest to the sudden change in the decay rate and robustness of correlations under phase-noise environments, a suitable initial state was prepared by mapping the NMR deviation matrix $\Delta\rho$ onto a Bell-diagonal state with $|c_1|, |c_2| > |c_3|$ on the right-hand side of (36). Figure 11 depicts the pulse sequence applied to monitor the correlation dynamics. With help of the deviation matrices obtained from quantum state tomography, the correlations were numerically computed at each time step $t_m = m/4J$ $(m = 0, 1, \ldots, 250)$.

The results in Fig. 12 clearly show the sudden change in the correlation decay rates, visible even under the strong influence of the thermal noise of the fluctuating fields in the nuclear spin environments. As pointed out

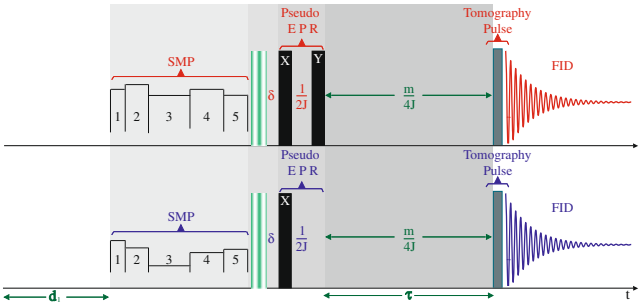

Fig. 11 (Color online) Pulse sequence implementing the dynamics of quantum and classical correlations under decoherence. The *bottom* (*top*) sequence corresponds to the representation of pulses applied to the ^{1}H (^{13}C) nuclei. First, the SMP technique and a z-gradient pulse implement a diagonal state. Next, a pseudo-EPR gate is performed. In the third step, the nuclear system and environment interact, resulting in decoherence of the quantum states. Finally, the quantum state is read out at equally spaced times $t_m = m/4J$ ($m = 0, 1, \ldots, 250$) with QST

in Section 2.4, the classical correlation should remain constant under phase damping. The weak decay in Fig. 12 is due to the thermal environment. Overall, the theoretical predictions agree well with the experiment.

The figure defines two decoherence regimes [31]. In the first regime, the decoherence affects more strongly the classical correlation; the quantum correlations decay, insignificantly. After the sudden change, the classical correlation becomes more robust against decoherence, while the quantum discord is progressively reduced by the noise. The experimental deviation matrices have small coherences, which introduce small oscillations in the recorded spectral line intensities. Small perturbations are consequently introduced in the linear

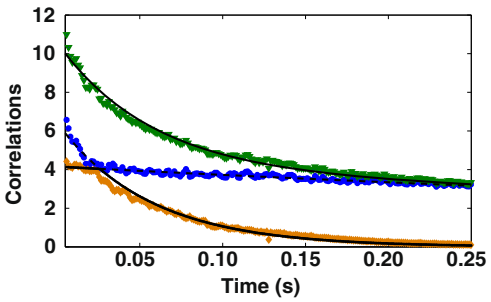

Fig. 12 (Color online) Sudden change in behavior and robustness of classical and quantum correlations under decoherence. The *filled triangles* (*green online*) depict the measured quantum mutual information. The *filled circles* (*blue online*) and *diamonds* (*orange online*) represent the classical and quantum correlations, respectively. The *solid lines* are the theoretical predictions. The initial state is analogous to the state defined by (36), with $|c_1|, |c_2| > |c_3|$. The correlations are displayed in units of $(\varepsilon^2/\ln 2)$bit

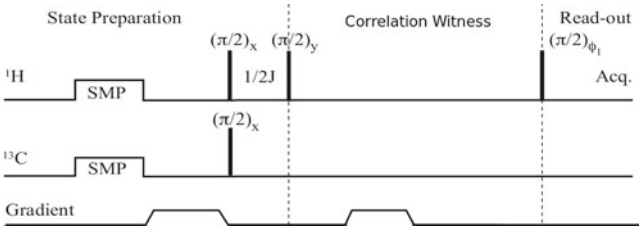

Fig. 13 Pulse sequence implementing the classicality witness. The *bottom* (*top*) sequence corresponds to the pulses applied to the ^{1}H (^{13}C) nucleus. In the first step, the SMP technique and a z-gradient pulse implement a diagonal state. In the second step, a pseudo-EPR gate is implemented. In the third step, the system interacts with the environment, which leads to decoherence of the quantum states. Finally, tomography reads out the quantum state at the uniformly distributed time intervals $m/4J$ ($m = 0, 1, \ldots, 11$)

system (67), which give rise to the oscillations in the experimental curves in Fig. 12.

3.4.2 Experimental Implementation of a Classicality Witness

Sections 3.3 and 3.4.1 dealt with QST measurements of quantum correlations. In certain situations, however, it suffices to identify the nature of correlations. For this purpose, correlations witnesses are convenient. As explained in Section 2.5, the space of classical states not being convex, linear witnesses are inadequate to identify the quantumness of correlations in separable states, and one must look for nonlinear witnesses. Here, we discuss an experimental implementation of the nonlinear classicality witness introduced in Section 2.5 [32]. The experiment used the same NMR apparatus that evidenced the sudden change of quantum discord under decoherence [35].

The pulse sequence implementing the classicality witness protocol is sketched in Fig. 13. Three states were prepared: a thermal equilibrium state ρ_{T}, a quantum-correlated state ρ_{QC}, and a classically correlated

Table 4 Witness, quantum discord, and classical correlation measured in three different initial states: the quantum correlated state ρ_{QC}, the classically correlated state ρ_{CC}, and the thermal equilibrium state ρ_{T}

	ρ_{QC}	ρ_{CC}	ρ_{T}
Witness	3.13	0.04	0.05
Quantum discord	4.02	0.00	0.00
Classical correlation	2.09	7.15	0.00

The witness was directly measured with the sequence of pulses in Fig. 13. The classical correlation and the symmetric quantum discord were computed by means of QST followed by numerical extremization. The correlations are displayed in units of $(\varepsilon^2/\ln 2)$bit

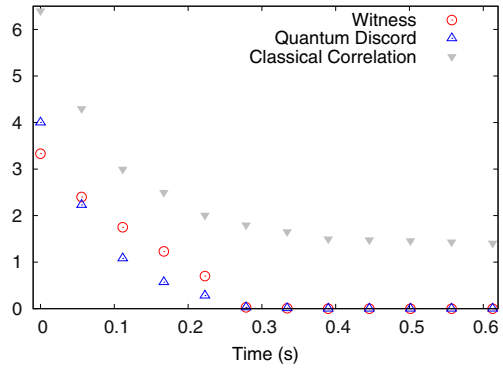

Fig. 14 (Color online) Measured witness and computed correlations for ρ_{QC} as a function of free-evolution time. Each *open circle* (*red online*) was obtained from a witness protocol carried out after the state had freely evolved for a time $t_n = n\delta t$ since initial preparation, where $\delta t = 55.7$ ms, and n is an integer ($0 \leq n \leq 11$). The *downward triangles* (*gray online*) indicate the amount of classical correlation, and the *upward triangles* (*blue online*) represent the symmetric quantum discord. The correlations are in units of $(\varepsilon^2/\ln 2)$bit

state ρ_{CC}. The measured values of the witness for the three different states are listed in Table 4. It is assumed that the classicality cutoff limit is $W_{\rho_T} = 0.05$, i.e., the equilibrium-state witness value. For the classical state, the witness value $W_{\rho_{CC}} = 0.04$ lies below the classicality cutoff. By contrast, the quantum-correlated state yielded $W_{\rho_{QC}} = 3.13$, which is far above the classicality bound 0.05. As this example shows, the classicality witness reliably sorts out quantum correlated states from classically correlated ones. For comparison, Table 4 also shows the quantum discord computed from the experimentally reconstructed deviation matrices, the result of QST followed by numerical extremization. As one would expect, while vanishing in the last two columns, which contain the witnesses within the classical bound, the QD is nonzero in the first column.

Finally, we discuss the decoherent dynamics of the witness. Following initial preparation in the state ρ_{QC}, we let the system evolve freely in the NRM environment during a time interval $t_n = n\delta t$, where $\delta t = 55.7$ ms and n is an integer, and then implement the witness protocol. The experimental results for $n = 0, 1, \ldots, 11$ are shown in Fig. 14, along with the correlations. The identification of classical states on the basis of the witness values agrees fairly well with the identification provided by the correlation quantifiers.

4 Concluding Remarks

Quantum information processing has the potential to promote advances not only in the foundations of physics, specially quantum mechanics and thermodynamics, but also in technology. Basic studies of quantum information therefore have great importance.

Quantum correlations are currently associated with the gain offered by quantum mechanics in comparison with classical protocols. Our understanding of the distinction between the quantum and the classical aspects of correlated system has dramatically changed since the seminal EPR paper in 1935 [1]. Initially, quantum correlations were identified with nonlocal aspects of quantum systems. After that, entanglement was raised to the status of quantum correlations. In the last decade, it was realized that even separable, nonentangled states can entail quantum correlations and hence carry an advantage in quantum information protocols that classical systems cannot match. The most popular quantifier of this kind of correlation is called quantum discord [15].

We have discussed the theoretical and the experimental aspects of quantum discord in NMR at room temperature. After dwelling on the dynamics of quantum discord under decoherence, we presented a witness for quantum correlation. The experimental investigations of both the QD and the witness were then surveyed, with a brief review of control techniques in NMR as well as of quantum state interrogation, a procedure known as quantum state tomography.

Acknowledgements The authors acknowledge the financial support from UFABC, CNPq, CAPES, FAPESP, FAPERJ, and Brazilian National Institute of Science and Technology for Quantum Information (INCT-IQ). The warm hospitality of Instituto de Física de São Carlos—Universidade de São Paulo (IFSC-USP) and Centro Brasileiro de Pesquisas Físicas (CBPF), where the experiments were performed, is also acknowledge.

References

1. A. Einstein, B. Podolsky, N. Rosen, Phys. Rev. **47**, 777 (1935)
2. E. Schrödinger, Proc. Camb. Philos. Soc. **31**, 555 (1935)
3. J.S. Bell, Physica **1**, 195 (1964)
4. J.F. Clauser, A. Shimony, Rep. Prog. Phys. **41**, 1882 (1978)
5. A. Aspect, http://arxiv.org/abs/quant-ph/0402001 (2004)
6. N.D. Mermin, Rev. Mod. Phys. **65**, 803 (1993)
7. R.F. Werner, Phys. Rev. A **40**, 4277 (1989)
8. S. Popescu, Phys. Rev. Lett. **72**, 797 (1994)
9. M.A. Nielsen, I.L. Chuang, *Quantum Computation and Quantum Information* (Cambridge University Press, Cambridge, 2000)
10. M. Piani, P. Horodecki, R. Horodecki, Phys. Rev. Lett. **100**, 090502 (2008)
11. C.E. Shannon, Bell Syst Tech J **27**, 379 (1948)
12. B. Schumacher, Phys. Rev. A **51**, 2738 (1995)
13. B. Groisman, S. Popescu, A. Winter, Phys. Rev. A **72**, 032317 (2005)
14. B. Schumacher, M.D. Westmoreland, Phys. Rev. A **74**, 042305 (2006)
15. H. Ollivier, W.H. Zurek, Phys. Rev. Lett. **88**, 017901 (2001)

16. L.C. Céleri, J. Maziero, R.M. Serra, Int. J. Quant. Inf. **9**, 1837 (2011)
17. K. Modi, A. Brodutch, H. Cable, T. Paterek, V. Vedral, Rev. Mod. Phys. **84**, 1655 (2012)
18. J.A. Jones, Prog. Nucl. Magn. Reson. Spectrosc. **59**, 91 (2011)
19. X.-h. Peng, D. Suter, Front. Phys. China **5**, 1 (2010)
20. S.L. Braunstein, C.M. Caves, R. Jozsa, N. Linden, S. Popescu, R. Schack, Phys. Rev. Lett. **83**, 1054 (1999)
21. G. Vidal, Phys. Rev. Lett. **91**, 147902 (2003)
22. R. Jozsa, N. Linden, Proc. R. Soc. Lond. A **459**, 2011 (2003)
23. N. Linden, S. Popescu, Phys. Rev. Lett. **87**, 047901 (2001)
24. A. Datta, A. Shaji, C.M. Caves, Phys. Rev. Lett. **100**, 050502 (2008)
25. V. Vedral, Found. Phys. **40**, 1141 (2010)
26. A. Datta, A. Shaji, Int. J. Quant. inf. **9**, 1787 (2011)
27. B. Eastin, http://arxiv.org/abs/1006.4402 (2010)
28. D.O. Soares-Pinto, R. Auccaise, J. Maziero, A. Gavini-Viana, R.M. Serra, L.C. Céleri, Phil. Trans. R. Soc. A **370**, 4821 (2012)
29. J. Maziero, L.C. Céleri, R.M. Serra, http://arxiv.org/abs/1004.2082 (2010)
30. J. Maziero, L.C. Céleri, R.M. Serra, V. Vedral, Phys. Rev. A **80**, 044102 (2009)
31. L. Mazzola, J. Piilo, S. Maniscalco, Phys. Rev. Lett. **104**, 200401 (2010)
32. J. Maziero, R.M. Serra, Int. J. Quant. Inf. **10**, 1250028 (2012)
33. D.O. Soares-Pinto, L.C. Céleri, R. Auccaise, F.F. Fanchini, E.R. deAzevedo, J. Maziero, T.J. Bonagamba, R.M. Serra, Phys. Rev. A **81**, 062118 (2010)
34. R. Auccaise, L.C. Céleri, D.O. Soares-Pinto, E.R. deAzevedo, J. Maziero, A.M. Souza, T.J. Bonagamba, R.S. Sarthour, I.S. Oliveira, R.M. Serra, Phys. Rev. Lett. **107**, 140403 (2011)
35. R. Auccaise, J. Maziero, L.C. Céleri, D.O. Soares-Pinto, E.R. deAzevedo, T.J. Bonagamba, R.S. Sarthour, I.S. Oliveira, R.M. Serra, Phys. Rev. Lett. **107**, 070501 (2011)
36. G.H. Aguilar, O. Jiménez Farías, J. Maziero, R.M. Serra, P.H. Souto Ribeiro, S.P. Walborn, Phys. Rev. Lett. **108**, 063601 (2012)
37. I.S. Oliveira, T.J. Bonagamba, R.S. Sarthour, J.C.C. Freitas, E.R. de Azevedo, *NMR Quantum Information Processing* (Elsevier, Amsterdan, 2007)
38. H. Kampermann, H.W.S. Veeman, J. Chem. Phys. **122**, 214108 (2005)
39. N. Sinha, T.S. Mahesh, K.V. Ramanathan, A. Kumar, J. Chem. Phys. **114**, 4415 (2001)
40. R.S. Sarthour, E.R. deAzevedo, F.A. Bonk, E.L.G. Vidoto, T.J. Bonagamba, A.P. Guimaraes, J.C.C. Freitas, I.S. Oliveira, Phys. Rev. A **68**, 022311 (2003)
41. F.A. Bonk, R.S. Sarthour, E.R. deAzevedo, J.D. Bulnes, G.L. Mantovani, J.C.C. Freitas, T.J. Bonagamba, A.P. Guimaraes, I.S. Oliveira, Phys. Rev. A **69**, 42322 (2004)
42. C.P. Slichter, *Principles of Magnetic Resonance* (Springer, Berlin, 1992)
43. K. Radley, L.W. Reeves, A.S. Tracey, J. Chem. Phys. **80**, 174 (1976)
44. G. Jaccard, S. Wimperis, G. Bodenhausen, J. Chem. Phys. **85**, 6282 (1986)
45. R. Auccaise, J. Teles, R.S. Sarthour, T.J. Bonagamba, I.S. Oliveira, E.R. deAzevedo, J. Magn. Reson. **192**, 17 (2008)
46. E. Knill, I.L. Chuang, R. Laflamme, Phys. Rev. A **57**, 3348 (1998)
47. D.G. Cory, M.D. Price, T.F. Havel, Physica D **120**, 82 (1998)
48. N. Gershenfeld, I.L. Chuang, Science **275**, 350 (1997)
49. N. Khaneja, R. Brochett, S.J. Glaser, Phys. Rev. A. **63**, 032308 (2001)
50. N. Khaneja, T. Reiss, C. Kehlet et al., J. Magn. Reson. **172**, 296 (2005)
51. E.M. Fortunato, M.A. Pravia, N. Boulant, G. Teklemariam, T.F. Havel, D.G. Cory, J. Chem. Phys. **116**, 7599 (2002)
52. J. Teles, E.R. deAzevedo, R. Auccaise, R.S. Sarthour, I.S. Oliveira, T.J. Bonagamba, J. Chem. Phys. **126**, 154506 (2007)
53. G.L. Long, H.Y. Yan, Y. Sun, J. Opt. B **3**, 376 (2001)
54. G.M. Leskowitz, L.J. Mueller, Phys. Rev. A **69**, 052302 (2004)
55. M. Cramer, M.B. Plenio, S.T. Flammia, R. Somma, D. Gross, S.D. Bartlett, O. Landon-Cardinal, D. Poulin, Y.-K. Liu, Nat. Commun. **1**, 149 (2010)
56. D.O. Soares-Pinto, M.H.Y. Moussa, J. Maziero, E.R. deAzevedo, T.J. Bonagamba, R.M. Serra, L.C. Céleri, Phys. Rev. A **83**, 062336 (2011)